using isotopically chiral (S)- and (R)-2 eight and six times, respectively (table S1, entries 25 to 32 and 33 to 38). The results show the same stereochemical correlations without any exception (23).

Finally, in series C of Table 1, (S)- and (R)-phenyl-1,2,3,4,5,6-$^{13}C_6$-phenylmethanol 3 were used as chiral initiators of asymmetric autocatalysis. When (S)-3 was used as the chiral trigger, enantioselective addition of i-Pr_2Zn to pyrimidine-5-carbaldehyde 4 afforded (S)-pyrimidyl alkanol 5 with 95% ee in 96% yield (entry 25). In contrast, the reaction in the presence of (R)-3 gave (R)-alkanol 5 with 92% ee (entry 26). These correlations between the ^{13}C isotope chirality and the configuration of the produced alkanol 5 also showed strong reproducibility, with (S)- and (R)-3 inducing the production of (S)- and (R)-5, respectively (Table 1, entries 27 to 32, and table S1, entries 39 to 46) (23).

In these enantioselective reactions, the initial formation of the zinc alkoxide of the isotopically chiral alcohol tips the enantiomeric balance of the initial i-Pr_2Zn addition to aldehyde 4; thus, a small enantiomeric excess of the zinc alkoxide of 5 is induced. After this step, the subsequent autocatalytic amplification of the small enantiomeric excess causes the zinc alkoxide of 5 to accumulate at enhanced ee, with an absolute configuration tied to that of the ^{13}C-labeled chiral alcohol (1, 2, or 3) used to trigger the process. Thus, the extremely small chiral effect generated by the substitution of the carbon isotope must be responsible, not for the amplification of the enantiomeric excess in the asymmetric autocatalysis, but for the enantioselection observed, that is, for the enantiomer produced in excess in the formation of the initial zinc alkoxide intermediate and therefore in the final production of 5.

Only minute energy differences can be associated with the isotopically substituted enantiomer of 1, 2, or 3 in causing the tiny enantiomeric excess of the alkoxide that triggers the asymmetric autocatalysis arising from the dialkylzinc addition to 4 (Fig. 2). It has been recognized that such minute energy differences are not interpretable with the tools available to structural theory (15, 31). In the initial reaction stage, the minute energy differences have a tiny effect, which is then cooperatively amplified to the final large enantiomeric excess. It is therefore impossible to disclose a structural reason for the difference in frequency of these initial enantiotopic face selectivities. The "cooperation–amplification" effect, which has been discussed regarding the structural effect of hydrogen deuterium chiral substitution in a helical polymer (15), finds reactive analogy in this autocatalytic system. The product handedness is entirely predictable, but the absolute value of the ee varies from run to run. This observation indicates a stochastic influence in the initiation phase biased by the chiral additive. The locally induced enantiomeric excess of zinc alkoxide is then amplified by the normal asymmetric autocatalytic process (32).

The neglected carbon isotopic chirality of many organic compounds on Earth—a characteristic that has largely eluded discrimination using contemporary methods—can thus be discriminated by asymmetric autocatalysis, which is a highly sensitive reaction for recognizing and amplifying the extremely small chiral influence between ^{12}C and ^{13}C. The method described above may expand the scope of research on carbon isotope chirality in organic molecules in nature (33). Natural enantiomeric excesses in this class of carbon isotopically chiral compounds may be very low, however. The possible role in asymmetric autocatalytic reactions of such compounds with low ee remains to be clarified.

References and Notes

1. K. Nakanishi, N. Berova, R. W. Woody, *Circular Dichroism: Principles and Applications* (Wiley, New York, 2000).
2. J. Haesler, I. Schindelholz, E. Riguet, C. G. Bochet, W. Hug, *Nature* 446, 526 (2007).
3. L. A. Nafie, T. B. Freedman, *Enantiomer* 3, 283 (1998).
4. L. D. Barron, *Nature* 238, 17 (1972).
5. K. Mislow, *Top. Stereochem.* 22, 1 (1999).
6. M. Tsukamoto, H. B. Kagan, *Adv. Synth. Catal.* 344, 453 (2002).
7. I. Weissbuch, L. Addadi, M. Lahav, L. Leiserowitz, *Science* 253, 637 (1991).
8. A. Eschenmoser, *Science* 284, 2118 (1999).
9. J. R. Cronin, S. Pizzarello, *Science* 275, 951 (1997).
10. M. A. Evans, J. P. Morken, *J. Am. Chem. Soc.* 124, 9020 (2002).
11. H. Pracejus, *Tetrahedron Lett.* 7, 3809 (1966).
12. I. Sato, D. Omiya, T. Saito, K. Soai, *J. Am. Chem. Soc.* 122, 11739 (2000).
13. A. Horeau, A. Nouaille, K. Mislow, *J. Am. Chem. Soc.* 87, 4957 (1965).
14. D. Arigoni, E. L. Eliel, *Top. Stereochem.* 4, 127 (1969).
15. M. M. Green et al., *Angew. Chem. Int. Ed.* 38, 3139 (1999).
16. K. Soai, T. Shibata, H. Morioka, K. Choji, *Nature* 378, 767 (1995).
17. I. Sato, H. Urabe, S. Ishiguro, T. Shibata, K. Soai, *Angew. Chem. Int. Ed.* 42, 315 (2003).
18. T. Shibata et al., *J. Am. Chem. Soc.* 120, 12157 (1998).
19. K. Soai et al., *J. Am. Chem. Soc.* 121, 11235 (1999).
20. T. Kawasaki et al., *J. Am. Chem. Soc.* 128, 6032 (2006).
21. D. G. Blackmond, C. R. McMillan, S. Ramdeehul, A. Schorm, J. M. Brown, *J. Am. Chem. Soc.* 123, 10103 (2001).
22. D. Lavabre, J.-C. Micheau, J. R. Islas, T. Buhse, *Top. Curr. Chem.* 284, 67 (2008).
23. Materials, methods, and additional experimental results of asymmetric autocatalysis are available as supporting material on *Science* Online.
24. O. Prieto, D. J. Ramón, M. Yus, *Tetrahedron Asymmetry* 14, 1955 (2003).
25. T. Katsuki, K. B. Sharpless, *J. Am. Chem. Soc.* 102, 5974 (1980).
26. O. Mitsunobu, M. Yamada, *Bull. Chem. Soc. Jpn.* 40, 2380 (1967).
27. K. Soai, S. Niwa, *Chem. Rev.* 92, 833 (1992).
28. G. Zhao, X. Li, X. Wang, *Tetrahedron Asymmetry* 12, 399 (2001).
29. K. Soai et al., *Tetrahedron Asymmetry* 14, 185 (2003).
30. T. Kawasaki, K. Suzuki, M. Shimizu, K. Ishikawa, K. Soai, *Chirality* 18, 479 (2006).
31. M. M. Green, C. Khatri, N. C. Peterson, *J. Am. Chem. Soc.* 115, 4941 (1993).
32. T. Shibata, S. Yonekubo, K. Soai, *Angew. Chem. Int. Ed.* 38, 659 (1999).
33. B. Barabás, L. Caglioti, K. Micskei, C. Zucchi, G. Pályi, *Orig. Life Evol. Biosph.* 38, 317 (2008).
34. This work was supported by a Grant-in-Aid for Scientific Research from The Ministry of Education, Culture, Sports, Science and Technology (MEXT). The authors are grateful to the reviewers for helpful discussions.

A Global View of the Lithosphere-Asthenosphere Boundary

Catherine A. Rychert* and Peter M. Shearer

The lithosphere-asthenosphere boundary divides the rigid lid from the weaker mantle and is fundamental in plate tectonics. However, its depth and defining mechanism are not well known. We analyzed 15 years of global seismic data using P-to-S (Ps) converted phases and imaged an interface that correlates with tectonic environment, varying from 95 ± 4 kilometers beneath Precambrian shields and platforms to 81 ± 2 kilometers beneath tectonically altered regions and 70 ± 4 kilometers at oceanic island stations. High-frequency Ps observations require a sharp discontinuity; therefore, this interface likely represents a boundary in composition, melting, or anisotropy, not temperature alone. It likely represents the lithosphere-asthenosphere boundary under oceans and tectonically altered regions, but it may constitute another boundary in cratonic regions where the lithosphere-asthenosphere boundary is thought to be much deeper.

Mapping the depth and character of the lithosphere-asthenosphere boundary with existing seismic methods has proven to be a challenge. Global surface-wave studies (1–4) image rigid lithospheres that increase in thickness from oceans to continents at broad

wavelengths (~1000 km). However, both the absolute depth and the nature of the boundary are debated. Lateral variations in depth likely occur at finer scales, as seen in regional results [e.g., (5, 6)]. Similarly, the depth resolution of most surface- and body-wave tomography studies is limited to >40 km, which is insufficient to determine the mechanism that defines the boundary. Finally, imaging of the boundary globally at higher resolution with regional and global stacks of body waves has not been possible (7). This could be because the boundary is not sharp enough to be detected at high frequencies, or because of small-scale variations in its depth and/or character. A growing number of regional observations of sharp velocity decreases with depth (P-to-S and S-to-P conversions; multibounce S waves) suggest the latter explanation in a variety of tectonic environments, such as beneath oceans (8), in hotspot regions (9, 10), and in continental regions with thin lithosphere (<110 km) (11–13). Beneath continental interiors, boundaries interpreted to be the base of the lid have been imaged using converted, reflected, or refracted phases; in many cases these dip to greater depths (>200 km) toward the continental interior [e.g., (14)], although the sharpness of the associated velocity gradient in these locations has not been determined and results beneath cratonic interiors can be relatively complex [e.g., (15, 16)]. Overall, sharp discontinuities associated with the tomographically defined lithosphere-asthenosphere boundary are detected in noncratonic regions, but they are not usually imaged beneath thick continental interiors. Therefore, although it is often assumed that the character of the boundary may vary, it has remained a puzzle as to why such a fundamental boundary would be so variable in its nature.

Here, we used Ps imaging to resolve the shear-wave velocity structure beneath individual seismic stations. We considered data in the IRIS (Incorporated Research Institutions for Seismology) FARM data set from 1990 to 2004 at single stations. We rotated the recorded wave field into its predicted P and S components before simultaneously deconvolving and migrating to depth (17) assuming a reference one-dimensional velocity model (IASP91). Our results are affected to some extent by crustal thicknesses and ratios of P-wave to S-wave velocity (V_P/V_S) that do not match IASP91, but reasonable variations in crustal parameters would change our results by <5 km in extreme cases and by <2.5 km generally (18). The same is the case for mantle V_P/V_S variations (11).

Of 745 stations, we focused on 334 with large quantities (>50 events) of high-quality

(signal-to-noise ratio >5) data. This amount of data is required to attain high-resolution imaging (i.e., clear signals owing to data stacking rather than low-pass filtering). We eliminated additional locations where deconvolved signals are characterized by ringing caused by noise and/or shallow discontinuities, and selected 169 stations that have relatively simple crustal structure—

that is, places where the Moho and its two first-order reverberations may be easily identified. This selection process was important for determining whether an observed phase is representative of discontinuity structure. An apparent phase in our deconvolved waveforms represents (i) the reverberation from a discontinuity at shallow depths, (ii) a side lobe of a crustal phase,
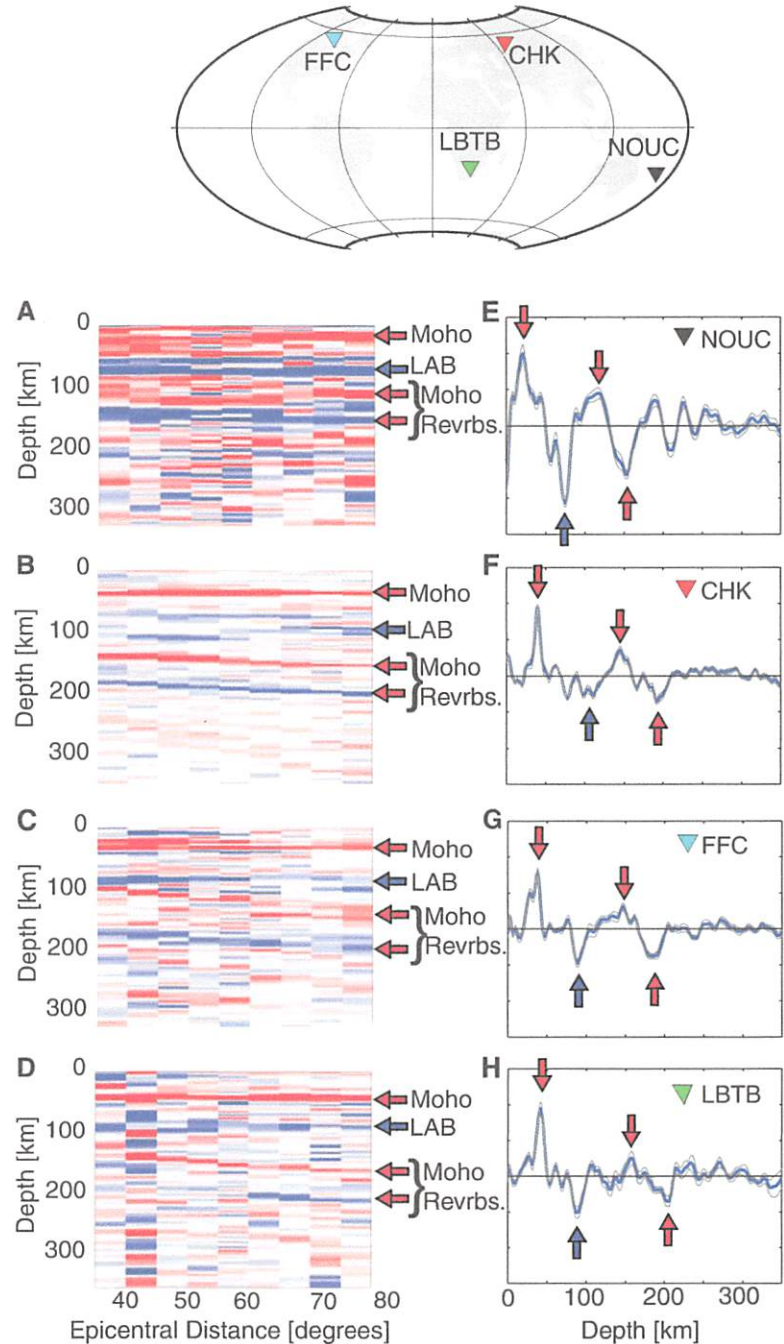

Fig. 1. Data examples for each tectonic region, after (19). Triangles on the map indicate station locations. Tectonic regions: NOUC, oceanic; CHK, Phanerozoic orogenic zones and magmatic belts; FFC, Phanerozoic platforms; LBTB, Precambrian shields and platforms. (**A** to **D**) Data binned by epicentral distance, with positive amplitude plotted in red and negative amplitude in blue. (**E** to **H**) All data from a given station deconvolved in a single bin (blue lines). Thin gray lines indicate 2σ error determined by bootstrap testing. Red arrows indicate crustal phases. Blue arrows indicate the phase we associate with the lithosphere-asthenosphere boundary (LAB).

Institute of Geophysics and Planetary Physics, Scripps Institution of Oceanography, University of California, San Diego, 9500 Gilman Drive, MC 0225, La Jolla, CA 92093, USA.

*To whom correspondence should be addressed. E-mail: crychert@ucsd.edu

or (iii) a direct conversion from a discontinuity at that depth. To evaluate these possibilities, we examined data binned by epicentral distance, which enables easy detection of crustal reverberations because they migrate to increasing depth with respect to epicentral distance. Once crustal phases were identified, we searched for other phases that may be associated with discontinuity structure. We also analyzed data stacked from all distances along predicted Ps moveout curves to enhance the visibility of the Ps phases that we observed.

At all stations where crustal phases were reasonably identifiable, we also found the presence of negative phases (i.e., phases opposite in polarity to the Ps conversion from the velocity increase at the Moho). These phases are not reverberations, because they do not migrate to increasing depth with respect to epicentral distance. In addition, the direct conversions and positive-polarity reverberations that would be associated with negative reverberation phases are not apparent. Furthermore, inclusion of high frequencies and consideration of epicentral distance and single bin plots indicate that the phases are distinct from surrounding phases and do not represent side lobes. Therefore, the observed negative phases likely represent direct conversions from sharp velocity drops at associated depths.

Our total data set included 14 stations from oceanic sites, 123 from Phanerozoic orogenic zones and magmatic belts, 14 from Phanerozoic platforms, and 18 from Precambrian shields and platforms (19) (Fig. 1). We rated the clarity of the waveforms and the certainty of identifying the phase of interest at each station, assigning ratings from 1 (most obvious) to 5 (most ambiguous) (18). Restricting the analysis to only the higher-quality ratings produced similar results to those presented here, but with less complete global coverage (fig. S2). At some stations, multiple phases that may be associated with discontinuities were observed (e.g., Fig. 1B). In these cases it is assumed that the deeper phase is the phase of interest and the shallower phase represents internal lithospheric structure, because it is unlikely that there is a velocity drop with depth within the sublithospheric mantle. Crustal reverberations can impede our ability to detect discontinuities at depths of ~100 to 200 km, depending on the thickness of the crust. We did not observe Ps phases related to sharp negative discontinuities between 200 and 410 km. Strong discontinuities between 100 and 200 km depth cause some degree of interference with reverberations, but this type of interference pattern was not observed consistently, either globally or beneath cratonic environments.

Depths to the discontinuity exhibited wide variation among individual stations, but most were between 60 and 110 km. We found a correlation between the depth of the observed discontinuity and tectonic environment when the results were plotted globally and results for locations in close proximity were simply averaged (Fig. 2). The average depth to the discontinuity in each of the tectonic environments increased from ocean to craton: 70 ± 4 km (oceans), 81 ± 2 km (Phanerozoic orogenic zones and magmatic belts), 82 ± 6 km (Phanerozoic platforms), and 95 ± 4 km (Precambrian shields and platforms). Averages of only the most reliable results (ratings 1 to 3) were within the estimated errors of the results that include all ratings (1 to 5). Our sampling of the oceanic lithosphere consisted entirely of ocean island stations and therefore may not be representative of typical oceanic lithosphere. The existence of multiple boundaries, primarily beneath magmatic/orogenic zones in our observations, could be the effect of non-coincident dehydration and depletion boundaries. A similar double boundary was imaged in eastern North America (12). We did not find a
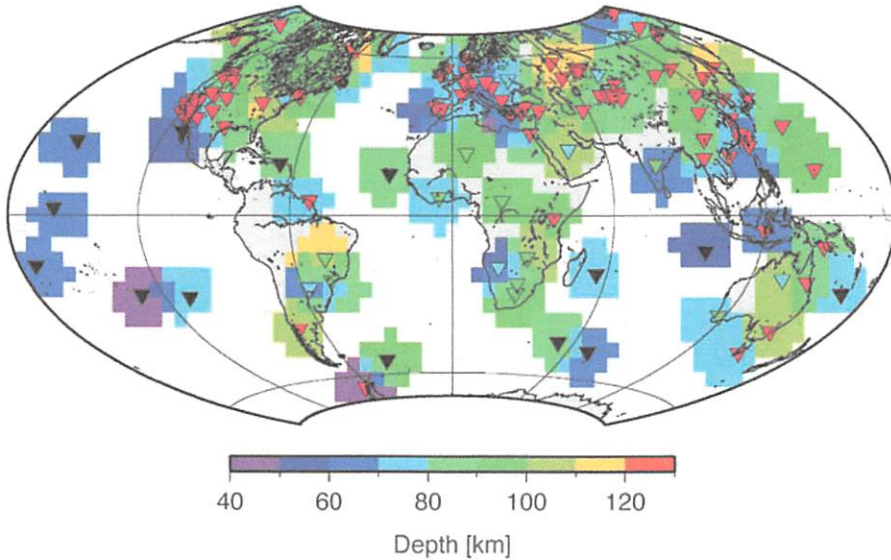

Fig. 2. Global map of the depth to the lithosphere-asthenosphere boundary imaged using *Ps*. Color indicates depth. Triangles show the 169 stations used in this study. Station color corresponds to tectonic regionalization, after (*19*); tectonic regions are colored as follows: black, oceanic; red, Phanerozoic orogenic zones and magmatic belts; cyan, Phanerozoic platforms; green, Precambrian shields and platforms. Although in (*19*) oceanic environments are divided into three age groupings, a single oceanic bin, encompassing all ages, is used here because sampling of this region is sparse.

Fig. 3. Comparison of *Ps*-inferred average properties of the lithosphere-asthenosphere boundary and Voigt averaged *S*-wave velocity profiles from the surface-wave results of (*2*) for different tectonic regions. The surface-wave profiles (*2*) are averaged tectonically over the entire model (dashed line) and beneath the stations used in this study (solid line). Horizontal lines represent average *Ps* results. Short solid vertical lines show estimated standard errors in average *Ps* depths. Separation between horizontal bars and vertical bars indicates errors in the average *Ps* magnitudes. Percentages are calculated with respect to the average surface-wave velocity at the *Ps* conversion depth in each region. Each panel represents a tectonic region (*19*) from left to right: oceanic, Phanerozoic orogenic zones and magmatic belts, Phanerozoic platforms, and Precambrian shields and platforms.
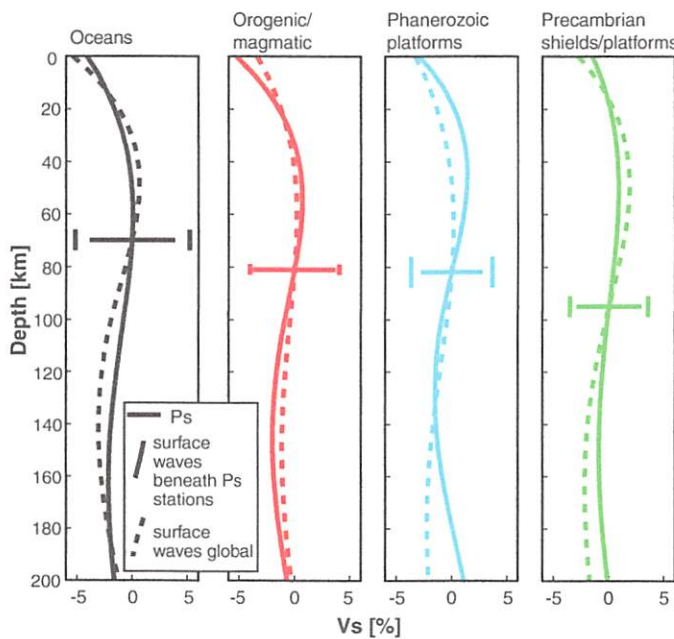
correlation between Moho depth and depth to this discontinuity.

The tectonically averaged Ps depths are similar to those of shear-wave velocity profiles from a recent surface-wave study (2) (Fig. 3). The Ps depths agree with the smooth decreases in surface-wave velocity beneath our stations: 70 ± 4 km versus a gradual decease from 61 to 164 km in oceanic environments, 81 ± 2 km versus 55 to 147 km beneath Phanerozoic orogenic zones and magmatic belts, 82 ± 6 km versus 46 to 130 km beneath Phanerozoic platforms, and 95 ± 4 km versus 51 to 152 km beneath Precambrian shields and platforms (Fig. 3). The surface-wave velocity drops in Fig. 3 are gradual, occurring over ~100 km, and a trend of increasing lithospheric thickness from ocean to craton is not apparent. However, surface waves average what is likely a more complicated velocity structure and can be relatively insensitive to the depth of the sharpest velocity contrast (5), which is the parameter to which Ps is sensitive. Our result is in agreement with the trend of increasing lithospheric thickness that is generally observed by global seismic results (1–4), although muted in magnitude.

The velocity contrast estimated for the Ps signal (18) is generally larger than the total drop in S-wave velocity from surface-wave studies (Fig. 3). The total Ps contrast decreases from $9 \pm 1\%$ beneath oceanic islands to $6 \pm 0.3\%$ beneath regions that have been tectonically altered to $6 \pm 1\%$ beneath both Phanerozoic and Precambrian platforms and shields, versus 2 to 6%, 3 to 4%, and 2 to 5% for the surface waves, respectively. However, strong, sharp contrasts are frequently observed on a regional scale. For instance, velocity drops of 3 to 9.6% over depths of less than 11 km at 60 to 110 km have been modeled beneath a variety of tectonic environments including fault zones, orogenic belts, passive continental margins, and oceanic plates (8, 11–13, 20). Global surface-wave results could be averaging a more complex structure consisting of lateral variations in the depth or character of this discontinuity, sharp negative vertical boundaries that occur within more gradual velocity increases with depth, or combinations of any or all of these phenomena.

Boundaries imaged by Ps at high frequency are sharp and cannot be explained by thermal gradients alone (11, 12); hence, they likely require a mechanism such as composition, melting, or anisotropy. Beneath continents, a boundary in depletion can explain velocity contrasts up to ~1.5% (21, 22) and a dehydration boundary may provide an additional ~4.5% (18), readily explaining the average Ps contrast (6%). Beneath oceans, a dehydration boundary may contribute up to 5.7% (18), slightly less than our observed 9%. However, the discrepancy could be caused by our sparse and biased sampling in oceanic regions (i.e., ocean islands only), a complex attenuation structure that is averaged by the global attenuation models (23) from which these numbers are derived, and/or the general low quality of the Ps ocean station results. Alternatively, a

small amount of partial melting in the asthenosphere (24–26) could easily produce a strong, sharp boundary (11) that is consistent with our results, although maintaining this amount of partial melting may be difficult because of melt connectivity.

Overall, either melting or composition could readily account for our observations, and beneath oceans and magmatic/orogenic regions, a weak asthenosphere at ~70 to 81 km depth seems reasonable in the context of global and regional seismic and geochemical evidence. However, beneath cratonic interiors, a weak asthenosphere from hydration or melting at ~95 km depth would likely induce lithosphere-asthenosphere decoupling, eliminating the possibility of a thermal boundary layer that extends to greater depths beneath continents. It is commonly accepted (27–29) that such a boundary layer is required to explain seismic evidence (1–4) that continental regions are seismically faster than oceanic regions at ~150 to 200 km depth.

One explanation is that the majority of our stations located on Precambrian shields and platforms are not actually sampling cratonic interiors. Many stations in the Precambrian shield/platform environment are located close to the boundaries between tectonic environments. A few stations with high-quality results (ratings of 1 to 3) are near the centers of cratons. However, in general the exact locations of cratonic roots at depth are somewhat ambiguous owing to the broad resolution of tomographic results. Alternatively, the discontinuities illuminated by this study beneath continents may represent boundaries in seismic anisotropy orientation or strength. Although a boundary in frozen-in anisotropy would not necessarily be associated with the lithosphere-asthenosphere boundary, such a feature would have implications for the formation and evolution of the continents. A sharp change from stronger to weaker radial anisotropy (i.e., transverse isotropy, vertical symmetry axis) with depth would produce a Ps phase with the correct polarity to explain our observations. Indeed, recent surface-wave results (2) indicate a decrease (~3%) in radial anisotropy from the Moho to ~125 km depth beneath Precambrian shields and platforms; this constitutes strong evidence that the observed boundary could be related to anisotropic structure beneath cratons. The strength of the anisotropy in this model alone is insufficient to explain our observed Ps amplitudes. However, as noted above, surface waves likely average more complicated structure.

An anisotropic explanation for our observations beneath oceans and magmatic/orogenic zones is not as likely. First, decreases in radial anisotropy with depth occur at deeper depths (>125 km) beneath the remaining tectonic environments in global surface-wave results (2). In addition, although sharp variations in anisotropy may be preserved in ancient structures in cratons, another mechanism (such as hydration or melt) would still be required to create sharp variations in

anisotropy beneath oceans and magmatic/orogenic zones. This same logic holds for creating a sharp boundary through variations in grain size (11).

A tectonically varying explanation for our globally pervasive Ps observations is not completely satisfying. However, in the context of global and regional tomography, this is the best explanation at the present time. Our results beneath oceans and Phanerozoic magmatic/orogenic zones likely represent a discontinuity in hydration or melting, and our results for shields and platforms either represent sampling at the edges of cratonic interiors or indicate that a sharp mid-lithospheric discontinuity in anisotropy is a global feature of cratonic roots.

References and Notes

1. M. Panning, B. Romanowicz, *Geophys. J. Int.* **167**, 361 (2006).
2. M. Nettles, A. M. Dziewonski, *J. Geophys. Res.* **113**, B02303 (2008).
3. S. Lebedev, R. D. van der Hilst, *Geophys. J. Int.* **173**, 505 (2008).
4. B. Kustowski, G. Ekstrom, A. M. Dziewonski, *J. Geophys. Res.* **113**, B06306 (2008).
5. A. B. Li, K. Burke, *J. Geophys. Res.* **111**, B10303 (2006).
6. F. J. Simons, A. Zielhuis, R. D. van der Hilst, *Lithos* **48**, 17 (1999).
7. P. M. Shearer, *J. Geophys. Res.* **96**, 18147 (1991).
8. Y. Tan, D. V. Helmberger, *J. Geophys. Res.* **112**, B08301 (2007).
9. X. Li, R. Kind, X. H. Yuan, I. Wolbern, W. Hanka, *Nature* **427**, 827 (2004).
10. X. Li *et al.*, *Nature* **405**, 938 (2000).
11. C. A. Rychert, S. Rondenay, K. M. Fischer, *J. Geophys. Res.* **112**, B08314 (2007).
12. C. A. Rychert, K. M. Fischer, S. Rondenay, *Nature* **436**, 542 (2005).
13. L. Chen, T. Y. Zheng, W. W. Xu, *J. Geophys. Res.* **111**, B09312 (2006).
14. P. Kumar, X. Yuan, R. Kind, G. Kosarev, *Geophys. Res. Lett.* **32**, L07305 (2005).
15. A. Levander, F. L. Niu, C. T. A. Lee, X. Cheng, *Tectonophysics* **416**, 167 (2006).
16. D. B. Snyder, *Tectonics* **27**, TC4006 (2008).
17. M. G. Bostock, *J. Geophys. Res.* **103**, 21183 (1998).
18. See supporting material on *Science* Online.
19. T. H. Jordan, *Bull. Seismol. Soc. Am.* **71**, 1131 (1981).
20. S. Oreshin, L. Vinnik, D. Peregoudov, S. Roecker, *Geophys. Res. Lett.* **29**, 1191 (2002).
21. C. T. A. Lee, *J. Geophys. Res.* **108**, 2441 (2003).
22. D. L. Schutt, C. E. Lesher, *J. Geophys. Res.* **111**, B05401 (2006).
23. C. A. Dalton, G. Ekstrom, A. M. Dziewonski, *J. Geophys. Res.* **113**, B09303 (2008).
24. H. Thybo, *Tectonophysics* **416**, 53 (2006).
25. D. L. Anderson, *Theory of the Earth* (Blackwell Science, Boston, 1989).
26. K. Mierdel, H. Keppler, J. R. Smyth, F. Langenhorst, *Science* **315**, 364 (2007).
27. C. T. A. Lee, A. Lenardic, C. M. Cooper, F. L. Niu, A. Levander, *Earth Planet. Sci. Lett.* **230**, 379 (2005).
28. S. D. King, *Earth Planet. Sci. Lett.* **234**, 1 (2005).
29. T. H. Jordan, *Nature* **274**, 544 (1978).
30. We thank J. Lawrence for preparing the seismogram data set, M. Nettles for providing her surface-wave model, and C. Dalton for providing her attenuation model.